Journal of
Composites Science

Article

Energy Absorption Mechanisms of Riveted and Assembled Double-Trapezoidal Auxetic Honeycomb Core Structures Under Quasi-Static Loading

Zhenhua Tian [1,2], Shaoqing Shi [1,2], Yu Liao [1,3,*], Wenkang Wang [1,3], Lei Zhang [1,2] and Yingjie Xiao [1,2]

[1] Army Logistics Academy of PLA, Chongqing 401331, China; t814822690@163.com (Z.T.); 17783074688@163.com (L.Z.)
[2] Key Laboratory of Military Underground Architectural Engineering, Chongging 401311, China
[3] Chongqing Key Laboratory of Emergency Fuel Supply Assurance and Oil & Gas Safety Safeguard, Chongqing 401331, China
* Correspondence: creast891230@163.com

Abstract: Auxetic honeycomb structures, known for their exceptional mechanical properties, are widely used as sacrificial layers to protect critical targets from extreme explosive loads. However, conventional double arrowhead auxetic honeycomb-core structures (DA-AHSs) encounter significant interfacial connectivity challenges, and scaling auxetic honeycombs with alternative cellular microstructures introduces further complexity. To overcome these issues, riveted and assembled double-trapezoidal auxetic honeycomb-core structures (DT-AHSs) were developed as a replacement for DA-AHSs. The deformation modes and energy absorption mechanisms of DT-AHSs were analyzed through theoretical methods and quasi-static testing. The results show that DT-AHSs energy absorption primarily relies on the yield deformation of the longer inclined walls and rotational deformation of the shorter inclined walls. Additionally, the shorter walls support auxetic behavior by stabilizing the deformation of the longer walls. These findings provide a basis for further exploration of the protective potential of DT-AHSs.

Keywords: honeycomb; negative Poisson's ratio effect; energy absorption; quasi-static; assembly-riveting method

Received: 4 January 2025
Revised: 12 February 2025
Accepted: 12 February 2025
Published: 14 February 2025

Citation: Tian, Z.; Shi, S.; Liao, Y.; Wang, W.; Zhang, L.; Xiao, Y. Energy Absorption Mechanisms of Riveted and Assembled Double-Trapezoidal Auxetic Honeycomb Core Structures Under Quasi-Static Loading. *J. Compos. Sci.* **2025**, *9*, 89. https://doi.org/10.3390/jcs9020089

1. Introduction

Recent terrorist attacks have shifted from traditional suicide bombings to more precise, smaller, and intelligent models [1]. This evolution creates new challenges for securing critical infrastructure, including weaponry, energy systems, and buildings. Research highlights that honeycomb materials featuring a negative Poisson's ratio exhibit significant potential for addressing these threats [2–7]. These auxetic honeycomb structures maintain the same basic composition as conventional honeycomb designs, incorporating an upper face-sheet, a core layer, and a lower face-sheet [8]. However, the core-layer exhibits a negative Poisson's ratio effect—often referred to as the auxetic effect—characterized by expansion when subjected to tension and shrinkage under compression [9–11]. This unique property sets it apart from structures with positive Poisson's ratios and enhances the shear modulus, compressive capacity, and energy absorption efficiency of traditional honeycomb configurations [12,13]. Furthermore, the auxetic effect promotes the formation of non-uniform porous structures within the honeycomb core before densification, thereby increasing the safety margin for structural protection [14].

Over the past few decades, auxetic honeycomb structures have diversified into various configurations such as chiral [15,16], star [17], concave hexagonal [18], and double arrowhead [19,20] shapes. Research by Qiu et al. [21] demonstrated that structures primarily undergoing bending deformation, such as hexagonal and rhombic types, exhibit a plateau in their stress–strain curves during quasi-static compression. In contrast, lattices such as square, triangular, and Kagome, which are dominated by thin-film deformation, display a sharp decline after reaching their peak values, lacking the plateau characteristic. Investigations into tetra-chiral (TC) honeycombs reveal that these structures also demonstrate non-uniform tensile and expansive deformations under quasi-static conditions [22]. Furthermore, Wei et al. [23] proposed a modeling approach for star honeycombs that addresses uncertainties in the elastic buckling or plastic collapse directions, thereby improving energy absorption. Studies from Ma et al. [14] demonstrated that double arrowhead auxetic honeycomb structures (DA-AHSs) enhance stress resistance, while Elipe and Lantada [24] found that both concave hexagonal and double arrowhead honeycombs present elastic moduli over ten times greater than other variants. Additionally, research by Hou et al. [25] and Gao et al. [26] confirmed the superior mechanical properties of DA-AHSs when compared to concave hexagonal structures, particularly regarding flexural and compressive resistance. Importantly, DA-AHSs can be manufactured in a single step, unlike concave hexagonal structures, which require secondary manual bending, attracting significant scholarly attention due to their exceptional mechanical properties under various loading conditions [27], including compression impact and blast.

Fabrication methods for DA-AHSs typically include 3D printing, wire cutting, and vacuum brazing. However, 3D printing is hampered by limitations related to part size and high costs, rendering it impractical for mass production and mainly suitable for small-scale specimens. Wire cutting, which involves carving structures from solid material, faces challenges in producing sharp angles and is primarily used for small components. In contrast, vacuum brazing offers advantages for mass production, enabling the seamless welding of prefabricated large and small “arrowhead” panels through the application of filler material, allowing for one-step interface bonding [8]. Despite this, commercial brazing furnaces can only accommodate weld seams under 600 mm, necessitating custom, energy-intensive, and expensive equipment for larger structures. Consequently, brazing is predominantly employed for intricate small-scale components. To address the needs of medium and large honeycomb structures, adhesive bonding and riveting are commonly used, though these methods encounter challenges related to line-to-line contact. Inspired by Yang and Ma’s [14] 3D double-U auxetic honeycomb structure, the design of DA-AHSs was modified by replacing the “arrow” configuration with a “platform” structure, transforming line-to-line contact into surface-to-surface contact. This modification led to the development of double-trapezoidal auxetic honeycomb core structures (DT-AHSs), which are formed by bending aluminum plates into high and low trapezoidal shapes and then assembled using rivets. The rivet holes are pre-drilled using laser cutting technology, which facilitates rapid on-site assembly and significantly improves the manufacturing efficiency of large-scale auxetic honeycomb structures.

Despite these advancements, research on the deformation behavior, energy absorption mechanisms, and mechanical properties of double-trapezoidal auxetic honeycomb structures (DT-AHSs) under quasi-static conditions remains limited. Notably, altering the geometry of the trapezoidal walls in DT-AHSs can transform their microstructure into either a two-dimensional diamond honeycomb core structure (2D-DHS) or a conventional hexagonal honeycomb core structure (CHHS). Both the 2D-DHS and CHHS represent structural topology variations within the broader “double-trapezoidal” auxetic framework. However, a rigorous comparison of the performance of DT-AHSs against these structural configurations has not yet been conducted, particularly concerning their mechanical properties and energy absorption capacities. Such comparisons are essential to elucidate the mechanical advantages of DT-AHSs under quasi-static loads.

This study establishes a three-phase investigation to elucidate the mechanical superiority of DT-AHSs. Phase I employs topological analysis to decode geometric transformation relationships among the DT-AHS, 2D-DHS, and CHHS. Phase II conducts quasi-static compression tests to comparatively analyze deformation modes across the three configurations, thereby validating the enhanced structural resistance of the DT-AHS. Phase III systematically varies the DT-AHSs geometric parameters (e.g., wall angles, lengths) to evaluate their influence on energy absorption efficiency and collapse mechanisms through additional compression experiments. The integrated findings aim to determine optimal design criteria and provide actionable guidelines for engineering applications of DT-AHSs in impact-resistant systems.

2. Theoretical Analysis

2.1. Structural Configuration

An aluminum plate was fabricated into a continuous high/low trapezoidal folding plate using a bending machine, as illustrated in Figure 1a. This continuous folding plate was then assembled and riveted to create the DT-AHSs, depicted in Figure 1b. By flipping the low trapezoidal folding plate of the DT-AHS, the structure transforms into a 2D-DHS, as shown in Figure 1c. Altering the inclined wall dimensions of the high/low trapezoidal folding plate results in the formation of a CHHS, illustrated in Figure 1d. The unit cell forms for the three honeycomb structures are presented in Figure 1e.

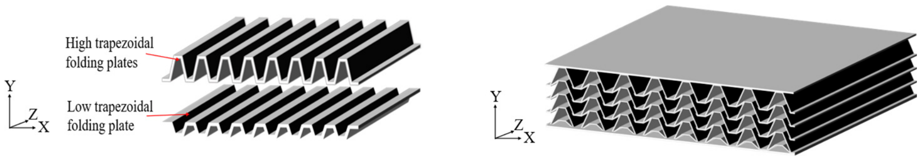

(**a**) 'High/Low' trapezoidal folding plate (**b**) DT-AHSs

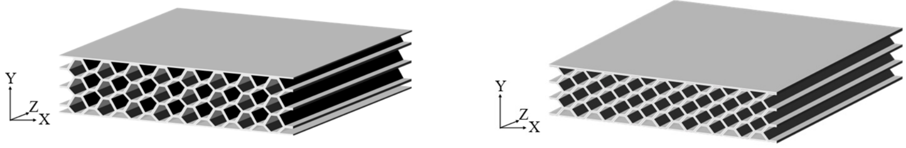

(**c**) 2D-DHSs (**d**) CHHSs

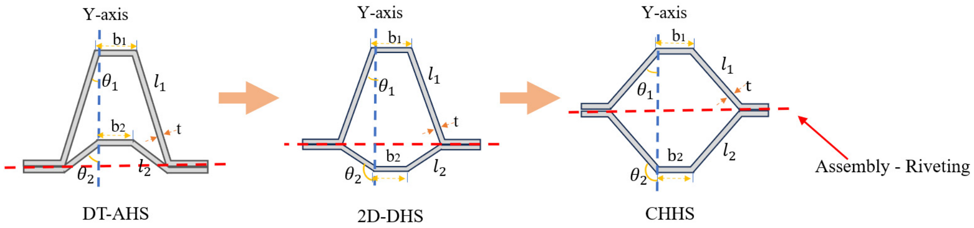

(**e**) unit cell and assembly riveting

Figure 1. Schematic of honeycomb structure and details of high/low 'trapezoidal' riveting variations.

To facilitate the analysis, the lengths of the inclined walls of the high/low trapezoidal structure are denoted as l_1 and l_2, where $l_1 \geq l_2$. The horizontal wall lengths are represented by b_1 and b_2, respectively. The angles between the inclined walls and the Y-axis are indicated as θ_1 and θ_2, with the constraints $0^\circ < \theta_1 < 90^\circ$ and $0^\circ < \theta_2 < 180^\circ$. Additionally, t represents the substrate thickness of the cell wall.

2.2. Stability Analysis

2.2.1. Theoretical Hypothesis

In this study, the horizontal walls between the cells are assumed to be riveted, forming monolithic structures. The bending stiffness of these walls increases by a factor of eight when the thickness is doubled. This observation suggests that the primary deformation occurs in the inclined walls, which can be extended along the X-, Y-, and Z-axes as needed. To simplify the analysis, the following assumptions are made:

(1) The horizontal wall of the target cell is treated as a rigid structure, with the analysis focusing solely on the deformation of the inclined walls and its effect on the Poisson's ratio of the target cell, so the inclined walls and horizontal walls are connected in a fixed way.

(2) The dimensions of the unit cell are assumed to be infinitely large in space, neglecting any boundary effects.

(3) The projection length of the honeycomb walls along the X-axis is influenced by wall thickness. However, this effect is small, and the projection lengths of the honeycomb walls are considered equal. Therefore, it is assumed that $l = l_1 \sin\theta_1 = l_2 \sin\theta_2$, with the condition $l_1 \geq l_2$.

(4) Symmetry considerations lead to the assumption that the horizontal motion of point A is negligible, and only vertical motion is taken into account.

(5) The analysis is limited to the small deformation stage, excluding any effects from additional bending moments or plastic deformation. When compressed, a simplified mechanical model based on these assumptions is presented in Figure 2.

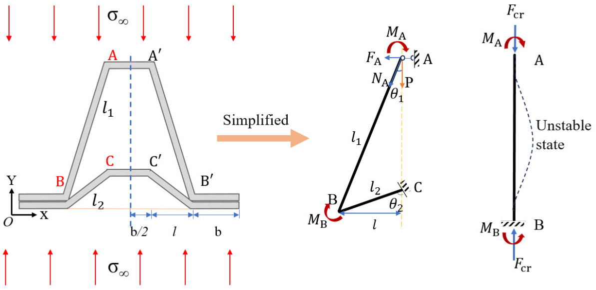

Figure 2. Simplified diagram of the unit cell model.

2.2.2. Static Stability Analysis of the Inclined Wall AB

When subjected to a uniform load along the Y-axis, the unit cell can be approximated as a concentrated downward force P acting at point A. This force P can be decomposed into two components: the axial pressure $N_A = P/\cos\theta_1$ and the horizontal force $N_X = P/\sin\theta_1$. Given the substantial stiffness and symmetry of the horizontal wall AA', the horizontal force N_X is equal to F_A. With small deformations, inclined wall AB experiences axial compression. Consequently, the stability analysis of inclined wall AB reduces to a simplified model with a fixed support at point A and B.

According to the strength of materials [28], when the slenderness ratio λ exceeds the critical value λ_p, the critical pressure F_{cr} for the compression rod can be calculated using Euler's formula:

$$F_{cr} = \left(\frac{2\pi}{l_1}\right)^2 EI = \frac{4\pi^2 EI}{l_1^2} \quad (1)$$

$$\sigma = F_{cr}/bt = \frac{4\pi^2 EI}{l_1^2 bt} \quad (2)$$

In Equation (1), E represents the elastic modulus and I is the moment of inertia, which for a rectangular beam is given by $I = b_z t^3/12$. Euler's formula is valid only when the critical stress remains below the proportional stress $\sigma_{\mathrm{P_0}}$, specifically $\sigma_{\mathrm{cr}} \le \sigma_{\mathrm{P_0}}$. The critical length of inclined wall AB can then be derived as follows:

$$l_1^{\mathrm{cr}} \ge \sqrt{\frac{\pi^2 E t^2}{3\sigma_{\mathrm{P_0}}}} \tag{3}$$

when $l_1 \ge l_1{}^{\mathrm{cr}}$, the critical force of AB, denoted as F_{cr}, can be calculated using σ_{cr} multiplied by the cross-sectional area. However, if $l_1 < l_1{}^{\mathrm{cr}}$, the minimum instability force cannot be determined using this equation. Instead, it must exceed F_{cr} according to the materials' mechanic principles.

2.2.3. Static Stability Analysis of the Inclined Wall BC

The static stability of the inclined wall BC is significantly influenced by angle θ_2. The force transmitted by the normal axis (N_{A}) can be decomposed into axial and normal components, as illustrated in Figure 3. This analysis identifies three distinct types of static actions: Figure 3a shows the tension–bending combination, Figure 3b depicts the compression–bending combination, and Figure 3c displays the bending moment only. Each type will be analyzed in the following sections.

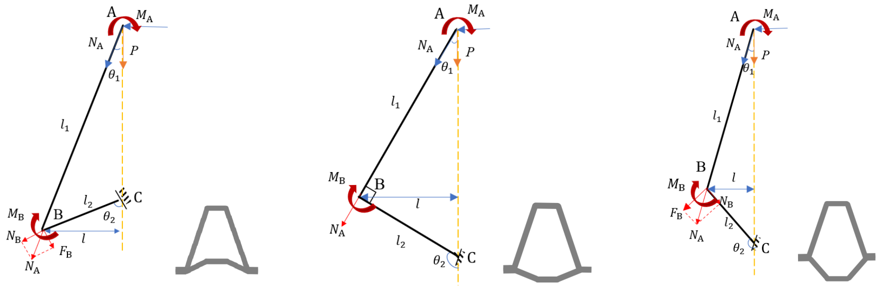

(**a**) $\theta_2 - \theta_1 < 90°$ (**b**) $\theta_2 - \theta_1 = 90°$ (**c**) $\theta_2 - \theta_1 > 90°$

Figure 3. Schematic diagram of unit cell and simplified analysis.

(a) Tension–bending combination (Figure 3a).

For the range $\theta_2 - \theta_1 < 90°$, the axial stress σ_{BC} and bending stress σ_{BM} acting on the inclined wall BC can be expressed as follows:

$$\sigma_{\mathrm{BC}} = \frac{N_{\mathrm{A}}\cos(\theta_2 - \theta_1)}{b_z t} \tag{4}$$

$$\sigma_{\mathrm{BM}} = \frac{M_{\mathrm{BC}}}{W_{\mathrm{BC}}} = \frac{6N_{\mathrm{A}}\sin(\theta_2 - \theta_1)x_2 - 6M_{\mathrm{B}}}{b_z t^2},\ 0 \le x_1 \le l_2 \tag{5}$$

where M_{BC} denotes the bending moment generated by F_{B}; W_{BC} denotes the section modulus in bending.

The maximum stress ($\sigma_{\max}$) in the BC due to both tensile and bending moments, located at point C, is given by the following:

$$\sigma_{\max} = \frac{N_{\mathrm{A}}\cos(\theta_2 - \theta_1)}{b_z t} + \frac{6N_{\mathrm{A}}\sin(\theta_2 - \theta_1)l_2 - 6M_{\mathrm{B}}}{b_z t^2} \tag{6}$$

Setting $\sigma_{\max} = \sigma_{\mathrm{P_0}}$, the corresponding normal force N_{A} can be determined:

$$N_{\mathrm{A}} = \left(\sigma_{\mathrm{P_0}} + \frac{6M_{\mathrm{B}}}{b_z t^2}\right) \Big/ \left(\frac{cos(\theta_2 - \theta_1)}{b_z t} + \frac{6sin(\theta_2 - \theta_1)l_2}{b_z t^2}\right) \tag{7}$$

Using the critical force F_{cr}, the ratio of N_{A} to F_{cr} can be expressed as follows:

$$\frac{F_{\mathrm{cr}}}{N_{\mathrm{A}}}=\frac{4\pi^2 EI}{l_1^2\left(\sigma_{\mathrm{P}_0}+\frac{6M_{\mathrm{B}}}{b_z t^2}\right)}\cdot\left(\frac{cos(\theta_2-\theta_1)}{b_z t}+\frac{6sin(\theta_2-\theta_1)}{b_z t^2}l_2\right) \tag{8}$$

$$\frac{F_{cr}}{N_A}=\frac{\pi^2 Etl_2}{3l_1^2\left(\sigma_{\mathrm{P}_0}+\frac{6M_{\mathrm{B}}}{b_z t^2}\right)}\cdot\left(\frac{t}{l_2}\cdot cos(\theta_2-\theta_1)+6sin(\theta_2-\theta_1)\right) \tag{9}$$

The value of $\theta_2-\theta_1$ represents the angle of the cell at point B. As $\theta_2-\theta_1$ decreases, the inclined walls l_1 and l_2 gradually converge. Within the range $10^\circ < \theta_2-\theta_1 < 90^\circ$, the following conditions hold: $l_2 > 1$ and $t > 0$. The maximum value of M_{B} is equal to the bending moment $M_{\mathrm{P}} = \sigma_{\mathrm{p0}}\mathrm{b_z t^2}/4$ at point B when the plastic yield is induced, and the minimum value of M_{B} is equal to zero.

Under these conditions, the inequality

$$\frac{t}{l_2}\cdot cos(\theta_2-\theta_1)+6sin(\theta_2-\theta_1)>1 \tag{10}$$

$$\frac{F_{cr}}{N_A}>\frac{\pi^2 Etl_2}{7.5l_1^2\sigma_{\mathrm{P}_0}}=\frac{\pi^2}{7.5}\cdot\frac{E}{\sigma_{\mathrm{P}_0}}\cdot\frac{tl_2}{l_1{}^2},\ M_{\mathrm{p}}\ =\ \sigma_{\mathrm{p0}}\mathrm{b_z t^2}/4 \tag{11}$$

$$\frac{F_{cr}}{N_A}>\frac{\pi^2 Etl_2}{3l_1^2\sigma_{\mathrm{P}_0}}=\frac{\pi^2}{3}\cdot\frac{E}{\sigma_{\mathrm{P}_0}}\cdot\frac{tl_2}{l_1{}^2},\ M_{\mathrm{p}}\ =\ 0 \tag{12}$$

Finally, $\frac{F_{cr}}{N_A} > \frac{\pi^2}{3}\cdot\frac{E}{\sigma_{\mathrm{P}0}}\cdot\frac{tl_2}{l_1{}^2}$ when there is a bending moment at point B.

(b) Bending moment only (Figure 3b).

In the case of a bending moment only, the maximum moment in the inclined wall BC is given by the following:

$$M_{\max}=N_{\mathrm{A}}l_2-M_{\mathrm{B}} \tag{13}$$

The corresponding $\sigma_{\max}$ is as follows:

$$\sigma_{\max}=\frac{M_{\max}}{W_{\mathrm{BC}}}=\frac{6N_{\mathrm{A}}l_2-6M_{\mathrm{B}}}{b_z t^2} \tag{14}$$

The yielding condition requires $\sigma_{\max}\geq\sigma_{\mathrm{p}}$, which leads to the following:

$$N_{\mathrm{A}}=\frac{b_z t^2}{6l_2}\left(\sigma_{\mathrm{P}_0}+\frac{6M_{\mathrm{B}}}{b_z t^2}\right) \tag{15}$$

The maximum value of M_{B} is equal to the bending moment $M_{\mathrm{P}} = \sigma_{\mathrm{p0}}\mathrm{b_z t^2}/4$ at point B when the plastic yield is induced, and the minimum value of M_{B} is equal to zero. So, the ratio of N_{A} and F_{cr} can be expressed as follows:

$$\frac{F_{\mathrm{cr}}}{N_{\mathrm{A}}}\geq\frac{4\pi^2 EI}{l_1^2}/\frac{b_z t^2}{6l_2}\left(\sigma_{\mathrm{P}_0}+\frac{6M_{\mathrm{B}}}{b_z t^2}\right)=0.8\pi^2\cdot\frac{E}{\sigma_{\mathrm{P}_0}}\cdot\frac{tl_2}{l_1{}^2},\ M_{\mathrm{p}}\ =\ \sigma_{\mathrm{p0}}\mathrm{b_z t^2}/4 \tag{16}$$

$$\frac{F_{cr}}{N_A}>\frac{2\pi^2 Etl_2}{l_1^2\sigma_{\mathrm{P}_0}}=2\pi^2\cdot\frac{E}{\sigma_{\mathrm{P}_0}}\cdot\frac{tl_2}{l_1{}^2},\ M_{\mathrm{p}}\ =\ 0 \tag{17}$$

Finally, $\frac{F_{cr}}{N_A} > 2\pi^2\cdot\frac{E}{\sigma_{\mathrm{P}0}}\cdot\frac{tl_2}{l_1{}^2}$ when there is a bending moment at point B.

(c) Compression and bending combination (Figure 3c).

For the case where $\theta_2 - \theta_1 > 90^\circ$, the axial stress σ_{BC} and bending stress σ_{BM} can be expressed as follows:

$$\sigma_{\mathrm{BC}} = \frac{N_{\mathrm{A}}\cos(\theta_1 + 180^\circ - \theta_2)}{b_z t} \tag{18}$$

$$\sigma_{\mathrm{BM}} = \frac{6N_{\mathrm{A}}\sin(\theta_1 + 180^\circ - \theta_2)x_2 - 6M_{\mathrm{B}}}{b_z t^2},\ 0 \le x_2 \le l_2 \tag{19}$$

The $\sigma_{\max}$ at point C, resulting from both the axial compression and bending moments, is as follows:

$$\sigma_{\max} = \frac{N_{\mathrm{A}}\cos(\theta_1 + 180^\circ - \theta_2)}{b_z t} + \frac{6N_{\mathrm{A}}\sin(\theta_1 + 180^\circ - \theta_2)l_2 - 6M_{\mathrm{B}}}{b_z t^2} \tag{20}$$

Setting $\sigma_{\max} = \sigma_{\mathrm{P}_0}$, the calculation formulation for N_{A} is as follows:

$$N_{\mathrm{A}} = \frac{\sigma_{\mathrm{P}_0} + \frac{6M_{\mathrm{B}}}{b_z t^2}}{\frac{\cos(\theta_1 + 180^\circ - \theta_2)}{b_z t} + \frac{6(N_{\mathrm{A}}\sin(\theta_1 + 180^\circ - \theta_2) + \mathrm{M}_0)}{b_z t^2} l_2} \tag{21}$$

The ratio of N_{A} and F_{cr} can be expressed as follows:

$$\frac{F_{\mathrm{cr}}}{N_{\mathrm{A}}} = \frac{\pi^2 E t l_2}{3l_1^2\left(\sigma_{\mathrm{P}_0} + \frac{6M_{\mathrm{B}}}{b_z t^2}\right)} \cdot \left(\frac{\mathrm{t}}{l_2} \cdot \cos\left(\theta_1 + 180^\circ - \theta_2\right) + 6\sin\left(\theta_1 + 180^\circ - \theta_2\right)\right) \tag{22}$$

As the value of θ_1 + 180° $- \theta_2$ decreases, the lengths l_1 and l_2 become progressively collinear. Within the range $10^\circ < \theta_1 + 180^\circ - \theta_2 < 90^\circ$, the following conditions hold: $l_2 > 1$ and $t > 0$. The maximum value of M_{B} is equal to the bending moment $M_{\mathrm{P}} = \sigma_{\mathrm{p0}} \mathrm{b_z t^2}/4$ at point B when the plastic yield is induced, and the minimum value of M_{B} is equal to zero.

From these parameters, the following inequality holds:

$$\frac{\mathrm{t}}{l_2} \cdot \cos\left(\theta_1 + 180^\circ - \theta_2\right) + 6\sin\left(\theta_1 + 180^\circ - \theta_2\right) > 1 \tag{23}$$

Further analysis leads to the following relationship:

$$\frac{F_{cr}}{N_A} > \frac{\pi^2 E t l_2}{7.5 l_1^2 \sigma_{\mathrm{P}_0}} = \frac{\pi^2}{7.5} \cdot \frac{E}{\sigma_{\mathrm{P}_0}} \cdot \frac{t l_2}{{l_1}^2},\ M_{\mathrm{p}} = \sigma_{\mathrm{p0}} \mathrm{b_z t^2}/4 \tag{24}$$

$$\frac{F_{cr}}{N_A} > \frac{\pi^2 E t l_2}{3 l_1^2 \sigma_{\mathrm{P}_0}} = \frac{\pi^2}{3} \cdot \frac{E}{\sigma_{\mathrm{P}_0}} \cdot \frac{t l_2}{{l_1}^2},\ M_{\mathrm{p}} = 0 \tag{25}$$

Finally, $\frac{F_{cr}}{N_A} > \frac{\pi^2}{3} \cdot \frac{E}{\sigma_{\mathrm{P}_0}} \cdot \frac{t l_2}{{l_1}^2}$ when there is a bending moment at point B.

A comparison of the three analyses reveals that the term $E/(\sigma_{\mathrm{P}_0})$ is a constant associated with the material properties. For aluminum alloy materials, the difference between E and σ_{P_0} is more than 600 times. Conversely, the term $t l_2/{l_1}^2$ represents geometric dimensions and is generally less than one. Thus, it is evident that $F_{\mathrm{cr}} > N_{\mathrm{A}}$. The results indicate that bending deformation in the inclined wall BC predisposes it to yield deformation in the inclined wall AB. This yielding occurs, causing rotation around point C and a downward movement in the direction of the N_{A}. Analysis of the fixed support at point A and the hinge at point C yields a consistent conclusion.

When compressed, the inclined walls bend initially at the endpoint before yielding. Geometrically, when $90^\circ < \theta_2 < 180^\circ$, the structure displays a positive Poisson's ratio; conversely, when $0^\circ < \theta_2 < 90^\circ$, an auxetic behavior is observed. To validate these theoretical considerations and extend their applicability to honeycomb design, a series of quasi-static compression tests will be conducted utilizing assembly-riveting techniques.

3. Quasi-Static Mechanical Property Comparison

3.1. Specimen Parameters

The honeycomb structure specimens are designed with dimensions of 250 mm × 250 mm × H, where the height (H) is influenced by core-layer parameters. This height is defined by the parameters $m \times n$, with m representing the number of cell columns in the X-direction and n representing the number of cell layers in the Y-direction, and ρ_{area} represents the areal density. The detailed structural parameters for three types of honeycomb structures are presented in Table 1 and Figure 4. The constant height constraint is implemented to meet the space requirements for target protection applications, such as vehicle chassis and energy-absorbing boxes.

Table 1. Detailed structural parameters for three types of honeycomb structures.

NO.	**Type**	$m \times n$	H (mm)	t (mm)	b_1 (mm)	b_2 (mm)	l_1 (mm)	l_2 (mm)	θ_1 (°)	θ_2 (°)	ρ_{area} (kg/m^2)
1	DT-AHS	8 × 5	69	0.5	8	8.6	16.6	7.4	25°	60°	26.6
2	2D-DHS	8 × 5	69	0.5	8	8.6	12.1	7.1	35°	107°	25.4
3	CHHS	8 × 5	69	0.5	8	8	9.0	9.0	50°	130°	24.7

DT-AHS 2D-DHS CHHS

Figure 4. Specimen diagram after riveting.

The thickness of the upper and lower face sheets is 1 mm, while the thickness of the core-layer substrate is 0.5 mm. All components are constructed from 1100 aluminum alloy, which is riveted using round-head M4 × 6 core-pulling steel rivets. The material properties for the 1100 aluminum alloy include a density of 2.7 g/cm^3, an elastic modulus of 69 GPa, a yield stress of 107 MPa, an ultimate stress of 206 MPa, and an elongation of 18.2%.

3.2. Evaluation Indicators

Six crashworthiness indicators are employed to evaluate the energy absorption capabilities of honeycomb structures: equivalent elastic modulus (E^*), initial yield stress (σ_{p}), plateau length ratio (*PLR*), plateau stress (σ_{pl}), plateau stress fluctuations (*PSF*), and specific energy absorption (*SEA*) [29–32].

3.2.1. Equivalent Elastic Modulus

E^* is defined as the slope of the elastic phase curve, which reflects the honeycomb's resistance to compressive deformation.

3.2.2. Initial Yield Stress

σ_{p} marks the transition of the honeycomb structure from the elastic phase to the plateau phase. This specific point corresponds to the yield strain, which is denoted as ε_{cr}.

3.2.3. Plateau Length Ratio

This ratio compares the length of the plateau to the height of the specimen. To determine this value, the dense strain (ε_{d}) of the honeycomb must first be established.

Energy absorption efficiency methods are commonly applied to measure the dense strain while minimizing human error and inertial effects. The efficiency is defined as follows:

$$\left.\frac{d\eta(\varepsilon)}{d\varepsilon}\right|_{\varepsilon=\varepsilon_{\mathrm{d}}} = 0 \tag{26}$$

Here, η represents the energy absorption efficiency to nominal stress corresponding to a specific strain:

$$\eta = \frac{\int_0^{\varepsilon} \sigma(\varepsilon) d\varepsilon}{\sigma(\varepsilon)} \tag{27}$$

where $\sigma(\varepsilon)$ denotes the stress and ε denotes the strain in the Y-direction of the honeycomb structure. Typically, the energy absorption efficiency curves display multiple peaks. At the point at which the energy efficiency curve begins, a marked decline is identified as the locked strain point, denoted as $\varepsilon_{\mathrm{cd}}$. The value of *PLR* can then be calculated using the following formula:

$$PLR = \frac{l_{\mathrm{pl}}}{H} = \frac{(\varepsilon_{\mathrm{cd}} - \varepsilon_{\mathrm{cr}}) \cdot H}{H} \tag{28}$$

where $\varepsilon_{\mathrm{cr}}$ denotes the strain at the yielding of the structure, and l_{Pl} denotes the plateau length.

3.2.4. Plateau Stress

After compressive yielding, the change in stress is minimal, while strain increases considerably. σ_{pl} is defined as the average stress in this region and must remain below the stress threshold of the protected structure as it reflects the primary energy absorption stage:

$$\sigma_{\mathrm{pl}} = \frac{\int_0^{\varepsilon} \sigma(\varepsilon) d\varepsilon}{\varepsilon} \tag{29}$$

3.2.5. Plateau Stress Fluctuations

PSF quantifies the extent of stress fluctuations during the crushing process, calculated as follows:

$$PSF = \frac{\int_{\varepsilon_{\mathrm{cr}}}^{\varepsilon_{\mathrm{cd}}} \left| \sigma(\varepsilon) - \sigma_{\mathrm{pl}} \right| d\varepsilon}{\int_{\varepsilon_{\mathrm{cr}}}^{\varepsilon_{\mathrm{cd}}} \sigma(\varepsilon) d\varepsilon} \tag{30}$$

3.2.6. Specific Energy Absorption

SEA measures the energy absorbed per unit mass, demonstrating the effectiveness of the honeycomb in energy absorption. It is calculated as follows:

$$SEA = \frac{\int_0^{\varepsilon} \sigma(\varepsilon) d\varepsilon \cdot s \cdot H}{M} \tag{31}$$

where M refers to the mass of the structure, and s represents the projection area of the honeycomb structure on the XZ plane.

3.3. Test Setup

Quasi-static compression tests were performed using a WAW-1000kN universal material testing machine (Tianshui Hong Shan Testing Machine, Tianshui, China), which consists of three main components: the universal testing machine control platform, the oil pump motor, and the control unit (see Figure 5). The specimen is accurately positioned at the geometric center of the test platform. Throughout the testing process, variations in force and displacement are monitored by sensors within the instrument and recorded in real time by a data acquisition system. Additionally, a fixed camera captured detailed footage of the entire compression test process. To minimize the influence of inertial effects on the evaluation of the structural mechanical properties, the loading speed is set to 0.5 mm/min during the elastic phase. Once the yield phase is reached, the compression rate is increased to 2 mm/min to enhance time efficiency [33,34].

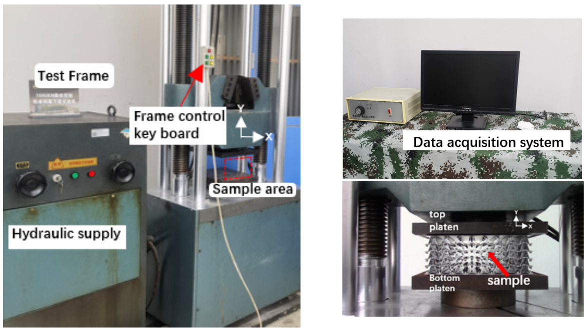

Figure 5. Compression test setup.

3.4. Results and Analysis

3.4.1. Deformation Mode

Figures 6 and 7 illustrate the deformation mechanisms of three honeycomb structures (DT-AHS, 2D-DHS, CHHS) and their local lateral cells under progressive equivalent strains. The red vertical dashed line represents the initial outer boundary, while the curved dashed line denotes the centerline of the outermost cell after compression (Subsequent markings are the same).

Firstly (ε = 0.28)**,** the DT-AHS undergoes shrinkage deformation characterized by the inward retraction of sidewalls (Figures 6b and 7b). Cell angles θ_1 and θ_2 decrease while walls l_1 and l_2 remain elastic, indicating initial bending and rotation of the inclined walls, as illustrated in Section 2.2.3(a). This yielding initiates at peripheral regions and propagates inward. In contrast, both the 2D-DHS and CHHS exhibit outward expansion with limited plasticity. Notably, the 2D-DHS shows restrained expansion, accompanied by θ_1 enlargement and θ_2 reduction without wall yielding. θ_1 becomes bigger and θ_2 becomes smaller without l_1 and l_2 yielded, meaning that the inclined walls of the cells first bend and rotate, as illustrated in Section 2.2.3(b,c).

Secondly (ε = 0.57), the DT-AHS demonstrates pronounced auxetic behavior and secondary porous reconfiguration (Figures 6c and 7c), significantly enhancing the structural resistance. The 2D-DHS displays similar auxetic but with attenuated shrinkage, while the CHHS experiences global expansion coupled with cell collapse. At this stage, l_1 and l_2 in all structures yield due to constrained angular reduction (θ_1, θ_2).

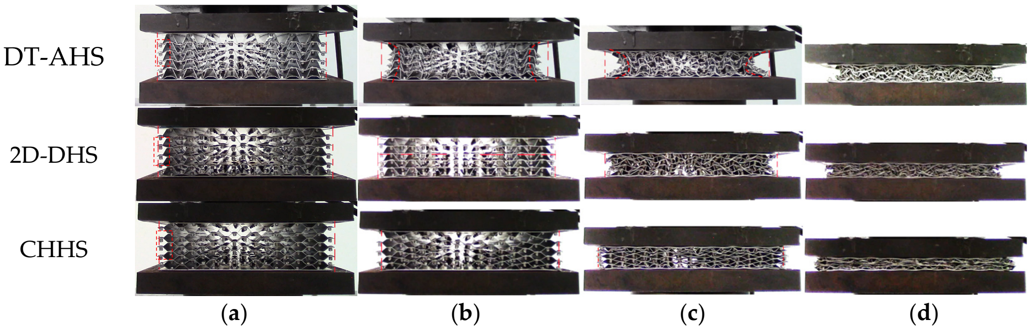

Figure 6. The deformation modes of three honeycomb structures: (**a**) undeformed state, (**b**) ε = 0.28, (**c**) ε = 0.56, (**d**) fully compressed dense state.

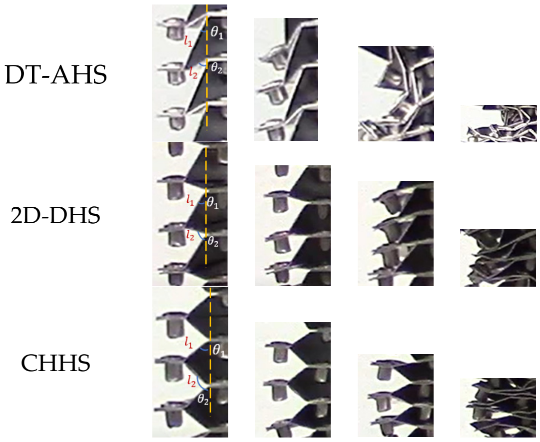

(**a**) (**b**) (**c**) (**d**)

Figure 7. The deformation diagram of the lateral cells of the structures highlighted in the red box in Figure 6: (**a**) undeformed state, (**b**) $\varepsilon = 0.28$, (**c**) $\varepsilon = 0.56$, (**d**) fully compressed dense state.

Final Compaction (Densified State): The DT-AHS and 2D-DHS develop concave cell edges with interlocking wall deformations, contributing to superior mechanical performance (Figures 6d and 7d). Conversely, the CHHS maintains orderly expansion with convex edges and aligned walls, lacking internal space for further deformation.

Comparative analysis reveals that central cells exhibit smaller θ_1/θ_2 variations but earlier yielding of l_1/l_2 walls. Central horizontal walls restrict inclined wall rotation, accelerating yielding, particularly pronounced in the DT-AHS (Figures 6 and 7). For the 2D-DHS and CHHS, compressive stresses induce lateral expansion insufficient to trigger wall yielding. In the DT-AHS, however, sustained tensile stresses during platform stages selectively constrain short walls (l_2) while promoting long wall (l_1) yielding, synergistically enhancing energy absorption and the load-bearing capacity.

3.4.2. General Stress–Strain Curves

The stress–strain characteristics of three honeycomb structures were evaluated through the energy absorption efficiency method, resulting in stress–strain curves that exhibit four distinct deformation zones (Figure 8): the linear elastic zone (Zone I), the plateau zone (Zone II), the plateau stress enhancement zone (Zone III), and the densification zone (Zone IV). In the figures, the purple dashed line indicates the initial yield point, the green dashed line delineates the boundary between the platform segment and the dense reinforcement zone, and the red line demarcates the boundary between the dense reinforcement zone and the dense reinforcement zone (Subsequent markings are the same).

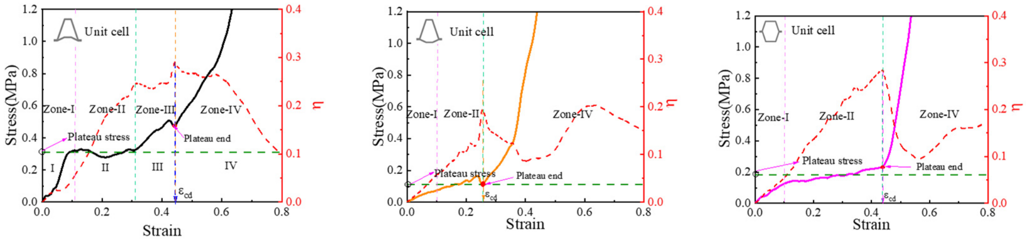

(**a**) (**b**) (**c**)

Figure 8. Nominal stress–strain curves and η–strain curves: (**a**) DT-AHS, (**b**) 2D-DHS, (**c**) CHHS.

In Zone I, stress increases linearly with strain, reflecting the structure's linear elasticity under compression. The CHHS and 2D-DHS curves exhibit similar low slopes, while the

DT-AHS demonstrates a steeper slope, indicating a higher E^*. The η–strain curves among the three structures show minimal variation in this zone.

Zone II begins with the yielding of the honeycomb structure. Stress plateaus and fluctuates as strain significantly increases. The DT-AHS curve initially shows a stress reduction, followed by a gradual rise. The 2D-DHS exhibits characteristics of both the CHHS and DT-AHS, starting with slow stress increases similar to the CHHS and transitioning into a sharp rise, leading to a secondary plateau. In this zone, the DT-AHS achieves the highest energy absorption efficiency, the CHHS performs moderately, and the 2D-DHS ranks the lowest.

Zone III lacks a clear boundary with Zone II. The first peak in the η–strain curves serve as the demarcation point. The CHHS and 2D-DHS show no distinct stress enhancement, while the DT-AHS displays a near-linear stress increase before transitioning into Zone IV, characterized by a steep increase in stress. The energy absorption efficiency of the DT-AHS reaches another peak in this zone.

In Zone IV, complete material densification occurs, leading to a rapid stress increase from the stress–strain curves. The CHHS experiences a sharp decline in the η–strain curve, while the DT-AHS maintains a plateau before gradually decreasing. The energy absorption of the 2D-DHS declines at a rate between that of the CHHS and DT-AHS.

Due to the unclear yielding thresholds for the CHHS and 2D-DHS, a yield strain of $\varepsilon_{cr} = 0.1$, derived from the DT-AHS, is used for comparison. Performance metrics such as E^*, σ_p, *PLR*, *PSF*, σ_{pl}, and *SEA* are listed in Table 2.

Table 2. Energy absorption performance indexes.

NO.	Type	ε_{cd}	E^* (MPa)	σ_p (MPa)	l_{pl} (mm)	*PLR*	*PSF*	σ_{pl} (MPa)	*SEA* (J/g)
1	DT-AHS	0.45	6.53	0.32	16	0.24	0.05	0.31	0.56
2	CHHS	0.44	1.21	0.13	23	0.34	0.15	0.16	0.19
3	2D-DHS	0.29	0.58	0.08	13	0.19	0.11	0.10	0.06

Figure 9 visualizes these data; the DT-AHS demonstrates superior performance across critical metrics—E^*, σ_p, and *SEA*—while maintaining minimal *PSF*. These attributes collectively enhance its energy dissipation capacity and mechanical stability. Although the DT-AHS exhibits a reduced l_{Pl}, its expanded platform reinforcement geometry enables the highest total energy absorption efficiency. In contrast, the CHHS delivers intermediate performance with extended l_{Pl} and moderate *SEA* values but lacks a defined stress enhancement zone. Notably, the 2D-DHS displays suboptimal stability under loading conditions, characterized by low platform stress distribution, truncated dimensions, and a rapid post-yield stress surge.

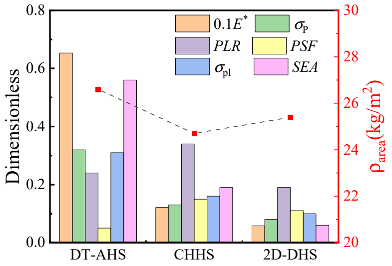

Figure 9. Comparison of energy absorption performance indices.

From a density perspective, the average ρ_{area} of the three structures is 25.5 kg/m^2. While the DT-AHS marginally exceeds this benchmark by 3.9%, its SEA value surpasses the average by 107.4%, underscoring its exceptional energy absorption-to-mass ratio. This pronounced efficiency advantage positions the DT-AHS as a technologically superior solution compared to both the CHHS and 2D-DHS.

In protective applications, a large number of scholars have obtained many valuable conclusions through static and dynamic experiments and numerical simulations, that is, ideal structures should offer strong load-bearing and energy absorption capacities while minimizing lateral expansion to protect adjacent modules from damage [1–7]. Based on overall performance, the DT-AHS is the most suitable structure for these protective scenarios among the three honeycomb configurations.

4. Parametric Analysis

Due to the superior mechanical properties of the DT-AHS compared to the CHHS and 2D-DHS, the latter two structures will not be considered in this study. The focus will be on investigating how various structural parameters of the DT-AHS affect its mechanical performance. The parameters examined include n, l_1, θ_1, l_2, and θ_2. For the baseline configuration, the following parameter values were chosen: l_1 = 16.6 mm, l_2 = 7.4 mm, θ_1 = 25°, and θ_2 = 60°. In this paper, the quasi-static compression test setup used is consistent with previous experiments performing a basic analysis. After mastering these parameters, dynamic performance tests and numerical simulation studies are needed to further optimize the parameters.

4.1. Parameter *n*

The number of core-layers (denoted by n) in the DT-AHS varies from 1 to 5. Figure 10 illustrates the deformation modes under different equivalent strain levels, with Figure 10a depicting the initial undeformed state. At an equivalent strain of $\varepsilon = 0.28$, the inclined walls (l_1 and l_2) begin to yield. For a single core-layer ($n = 1$), the lower trapezoidal walls (l_2) are fixed to the lower face sheets, restricting their deformation. Only l_1 yields, and no inward shrinkage occurs. Increasing the number of core-layers introduces inward shrinkage in l_2, resulting in an auxetic effect, as demonstrated in Figure 10b. At an equivalent strain of $\varepsilon = 0.57$, l_1 undergoes further compression, while l_2 offers resistance, stabilizing the deformation of l_1 (Figure 10c). In the fully compressed state, the cells interlock, enhancing the structure's stiffness and resistance, as shown in Figure 10d. This interlocking behavior, referred to as a mixed dense state, becomes more pronounced with higher n, significantly improving the mechanical performance of the DT-AHSs.

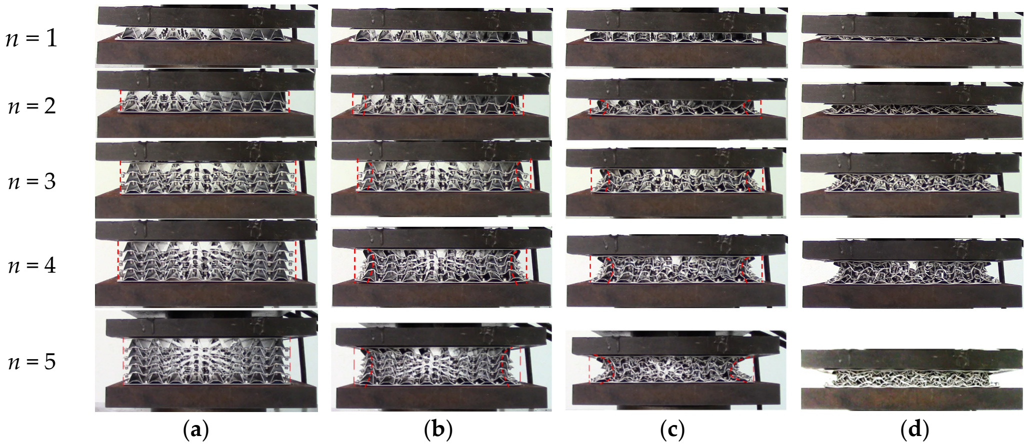

Figure 10. The deformation modes of DT-AHSs with different layers: (**a**) undeformed state, (**b**) $\varepsilon = 0.28$, (**c**) $\varepsilon = 0.56$, (**d**) fully compressed dense state.

Figure 11 presents the stress–strain and η–strain curves for DT-AHSs with different n-values. As n increases, both the yield stress and the influence of rivet-induced local protrusions on deformation decrease. For n = 1 (Figure 11a), the l_2 walls contribute to a significant stress increase after yielding. This results in large stress fluctuations in the plateau region and the absence of a stress reinforcement zone.

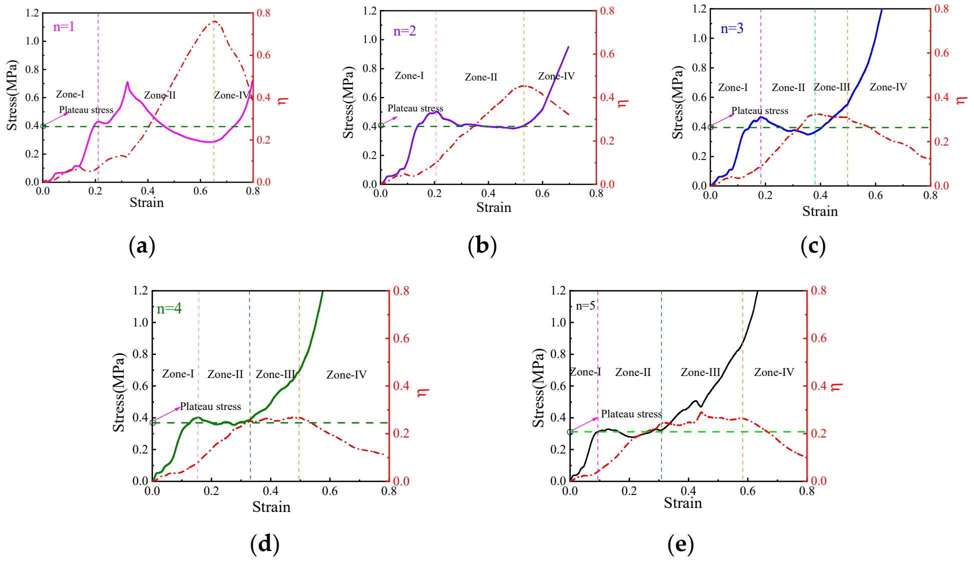

(**a**) (**b**) (**c**)

(**d**) (**e**)

Figure 11. Stress–strain and η–strain curves of DT-AHSs with varying n-values (**a**) n = 1, (**b**) n = 2, (**c**) n = 3, (**d**) n = 4, (**e**) n = 5.

For n = 2 (Figure 11b), a distinct stress plateau appears, and stress fluctuations are minimal, although a reinforcement zone remains absent. When n increases further, the deformation behavior divides into four distinct zones, as shown in Figure 11c–e.

- Zone I: The η-values remain low for all configurations, with no significant differences observed.
- Zone II: Rapid η growth is exhibited by the single-layer structure, achieving a high level. Among multi-layer configurations, the five-layer structure (n = 5) demonstrates the best energy absorption performance.
- Zone III: For n = 5, the η–strain curves display an extended plateau, reflecting sustained energy absorption.
- Zone IV: A gradual decline in the η–strain curves is observed as n increases, indicating reduced efficiency for configurations with more layers.

Figure 12 highlights the energy absorption performance indices of DT-AHSs with different n-values. The E^* remains nearly constant, with deviations below 10%, and reaching its maximum value at n = 2. However, the σ_p decreases more notably compared to the σ_{pl}, and the *PLR* shows a slight reduction. Conversely, the force-smoothing characteristics and *SEA* capacity gradually improve with an increasing number of layers, and *SEA* achieves its peak at n = 5.

As the number of layers rises, the ρ_{area} increases linearly. Combined with the analysis in Figure 9, it can be found that the deformation of the cellular cells linked to the top and bottom plates is severely limited. The more honeycomb cores in the middle facilitates l_1 yielding and l_2 shrinkage, resulting in a lower yield point and an extended plateau zone. The plastic deformation of cells riveted to the upper and lower face sheets remains limited. In contrast, cells closer to the middle core-layers undergo more complete plastic deformation, enabling higher impact energy absorption. This progression demonstrates that an increase in the number of layers enhances the energy absorption performance of the DT-AHS.

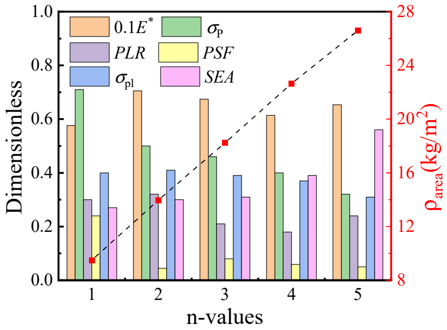

Figure 12. Influence of *n*-values on energy absorption performance indices.

4.2. Parameter l_1

Based on the baseline parameters for the DT-AHS, l_2 remains constant while the l_1 values are adjusted to 14.0 mm, 16.6 mm, 20.5 mm, and 27.0 mm. The corresponding θ_1 values for these configurations are 30°, 25°, 20°, and 15°, respectively. The DT-AHS configurations are designated as DL1-01, DL1-02, DL1-03, and DL1-04.

Figure 13 illustrates the instantaneous deformation of these configurations under different equivalent strains. Smaller l_1 values result in reduced internal pore sizes (Figure 13a), leading to easier densification of the core-layer. However, limited plastic deformation prevents full utilization of the material's deformation capacity. In contrast, excessively large l_1 values cause antisymmetric yielding and shear slip within the structure as indicated by the red dashed arrow in Figure 13b. This reduces the auxetic effect and leads to the outward protrusion of side cells, as observed in DL1-03 and DL1-04 (Figure 13c). Under full compression (Figure 13d), the sides of DL1-04 protrude outward, while the sides of DL1-01, DL1-02, and DL1-03 exhibit inward shrinkage. Smaller l_1 values result in more pronounced inward shrinkage deformation.

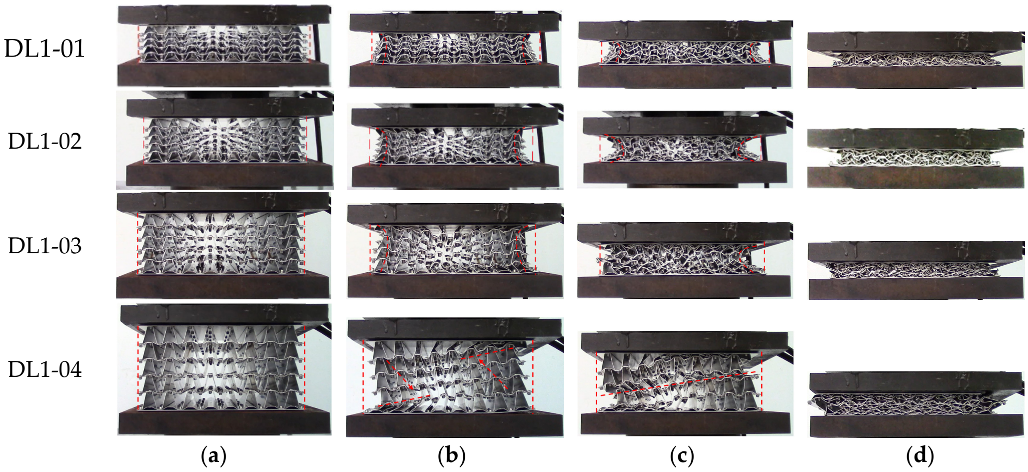

(**a**) (**b**) (**c**) (**d**)

Figure 13. The deformation modes of DT-AHSs with different l_1: (**a**) undeformed state; (**b**) $\varepsilon = 0.28$; (**c**) $\varepsilon = 0.56$; (**d**) fully compressed dense state.

Figure 14 compares the stress–strain and η–strain curves across varying l_1 values. The E^* shows minimal variation. However, both σ_p and σ_{pl} decrease progressively with increasing l_1. The proportion of the plateau segment increases as l_1 grows. At smaller l_1 values, the plateau region is absent (Figure 14a). As l_1 increases, σ_{pl} variations become less significant (Figure 14b,c). At $l_1 = 27.0$ mm, no stress reinforcement zone is observed (Figure 14d).

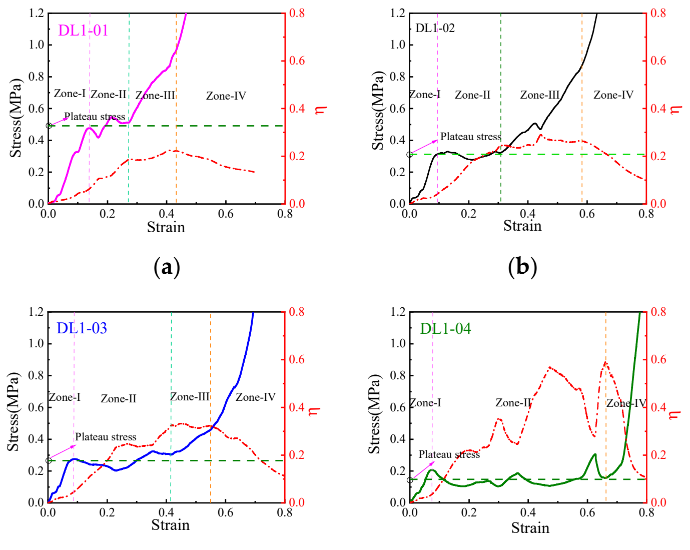

(**a**) (**b**)

(**c**) (**d**)

Figure 14. Nominal stress–strain curves and η–strain curves of DT-AHSs with different l_1: (**a**) DL1-01, (**b**) DL1-02, (**c**) DL1-03, (**d**) DL1-04.

The η–strain curves across different deformation zones reveal distinct trends.

- Zone I: The growth rate of the η-value is similar.
- Zone II: The η-value grows more rapidly as l_1 increases, with longer l_1 producing higher peak energy efficiency values.
- Zone III: The η-value features an extended plateau segment for configurations with larger l_1, indicating superior sustained energy absorption.
- Zone IV: The η-value decreases gradually as l_1 increases, reflecting reduced energy absorption in the later stages of deformation.

These results demonstrate that varying l_1 significantly influences the deformation modes, stress–strain behavior, and energy absorption performance of DT-AHSs. Smaller l_1 values favor inward shrinkage, while larger l_1 values enhance plateau segment development but may lead to reduced overall efficiency.

Figure 15 illustrates the energy absorption performance indices of DT-AHSs with varying l_1 values. As l_1 increases, E^*, σ_p, and σ_{pl} decrease significantly. Compared to DL1-04, DL1-01 demonstrates a 75% higher E^*-value, a 100% higher σ_p-value, and a σ_{pl}-value more than 200% greater. DL1-02 has a larger E^* and an optimal *SEA*. However, the proportion of the *PLR* increases linearly with l_1.

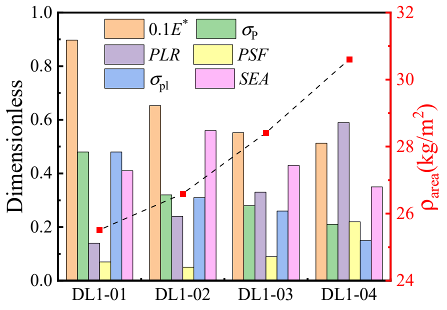

Figure 15. Effect of changing l_1 on the energy absorption properties.

The total energy absorption does not follow a linear trend but fluctuates with l_1. At l_1 = 16.6 mm, the *SEA* efficiency and force stability reach their peak values. Excessively large l_1 values, however, fail to enhance plastic deformation effectively. Instead, they increase the overall mass and reduce structural stability. Higher l_1 values also lead to premature yielding under smaller external forces. The bending moment in the platform section rises, strengthening the resistance of l_2 to deformation. However, this results in uneven internal stress distribution within the core-layer. Consequently, deformation becomes less predictable, with torsion and slip commonly observed. These findings suggest that optimizing l_1 is crucial to balancing energy absorption performance and structural stability.

4.3. Parameter l_2

Based on the baseline parameters for the DT-AHS, l_1 remains constant while the l_2 values are adjusted to 6.30 mm, 6.80 mm, 7.40 mm, 8.40 mm, and 10.00 mm. The corresponding θ_2 values for these configurations are 90°, 70°, 60°, 50°, and 40°, respectively. The DT-AHSs configurations are designated as DL2-01, DL2-02, DL2-03, DL2-04, and DL2-05.

Figure 16 shows the instantaneous deformations of DT-AHSs under varying equivalent strains for different l_2 values. As l_2 increases, the internal space within the core-layer decreases, as illustrated in Figure 16a. During compression, all five configurations exhibit concave side deformations (Figure 16b). The degree of concavity becomes more pronounced with further compression (Figure 16c). Additionally, all structures demonstrate a strong auxetic effect (Figure 16d).

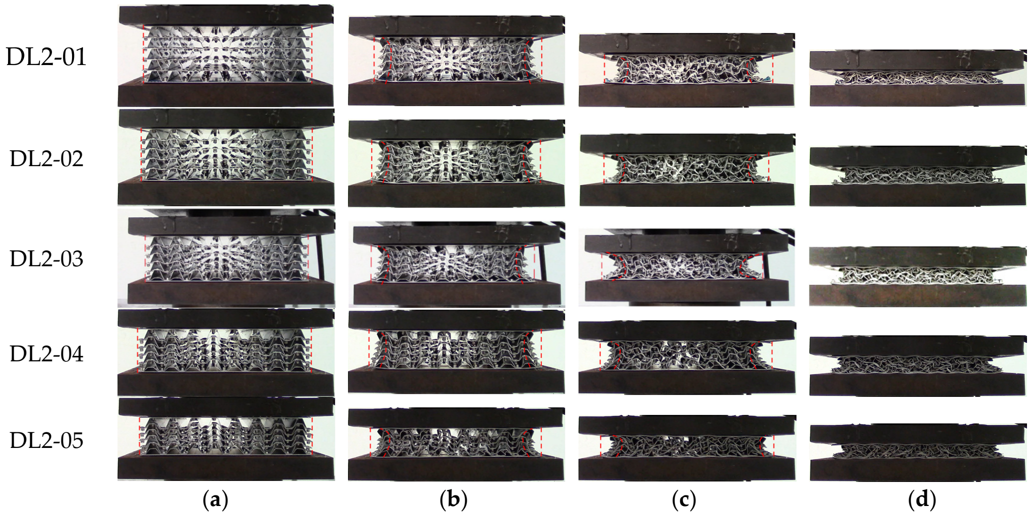

Figure 16. The deformation modes of DT-AHS with different l_2: (**a**) undeformed state, (**b**) ε = 0.28, (**c**) ε = 0.56, (**d**) fully compressed dense state.

Figure 17 presents the stress–strain and η–strain curves for the DT-AHSs with different l_2 values. When l_2 is small, the structure exhibits a low E^*, large elastic strain, and lacks a stress reinforcement zone (Figure 17a). As l_2 increases, both E^* and σ_p rise, while the plateau zone becomes narrower, as seen in Figure 17b,c. The proportion of stress enhancement zones also increases significantly.

However, when l_2 becomes excessively large, the internal core space reduces further. This leads to a rapid increase in stress with strain and causes the structure to densify quickly, as demonstrated in Figure 17d,e. These findings emphasize the critical role of optimizing l_2 values to balance deformation control, stress distribution, and energy absorption performance in DT-AHS.

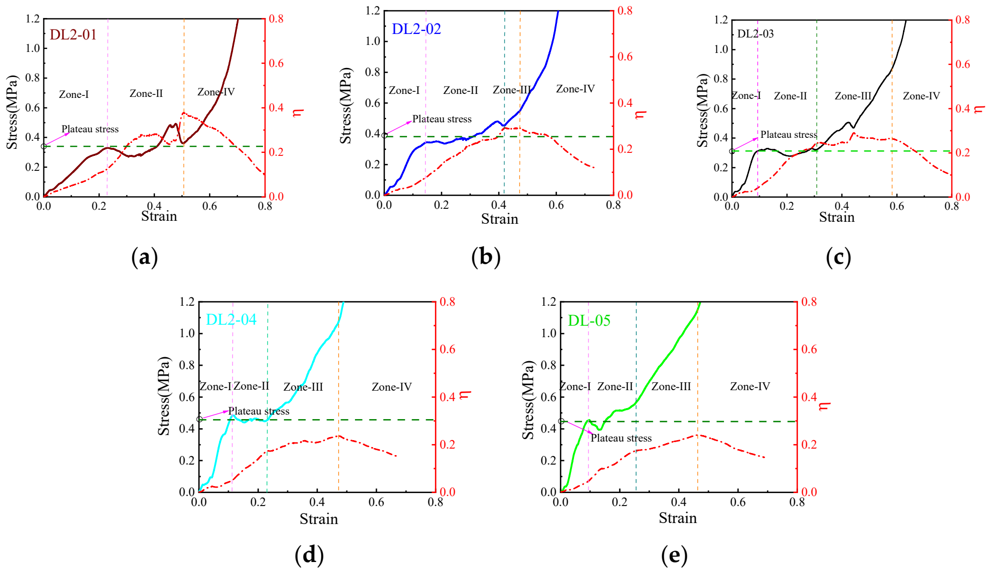

(**a**) (**b**) (**c**)

(**d**) (**e**)

Figure 17. Nominal stress–strain curves and η–strain curves of DT-AHSs with different l_2: (**a**) DL2-01, (**b**) DL2-02, (**c**) DL2-03, (**d**) DL2-04, (**e**) DL2-05.

Figure 18 shows that as l_2 increases, both ρ_{area} and E^* rise. The *SEA* characteristics and four other performance indices display a fluctuating trend, with peak values occurring at intermediate l_2. At l_2 = 7.4 mm, the *SEA* efficiency reaches its maximum, along with improved force stability. Excessively large l_2 values, however, fail to promote sufficient plastic deformation and lead to increased overall mass. Conversely, smaller l_2 values result in smaller E^* and the absence of a stress reinforcement zone.

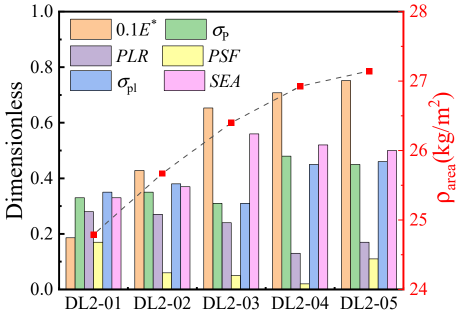

Figure 18. Effect of changing l_2 on the energy absorption properties.

This behavior can be explained as follows: in the elastic deformation zone, l_2 primarily undergoes bending and rotation, which generates lower resistance compared to the plastic yield deformation of l_1. As l_2 increases, the overall height of the DT-AHS decreases, restricting the deformation of honeycomb cells. Consequently, the core-layer densifies rapidly, limiting the structure's ability to achieve high energy absorption efficiency.

SEA serves as a critical performance metric for evaluating honeycomb structures. As evidenced by the parametric analysis presented in Figure 18, a comparative study of the geometric parameter effects reveals distinct nonlinear correlations between l_1 (θ_1) and l_2 (θ_2) in modulating the energy absorption efficiency of the DT-AHSs. The influence curve for l_1 (θ_1) shows a much steeper trend compared to l_2 (θ_2), as seen in Figure 19a,b. This stark contrast highlights the dominant role played by l_1 (θ_1) in regulating energy absorption performance, whereas changes in l_2 (θ_2) exert a relatively minor impact.

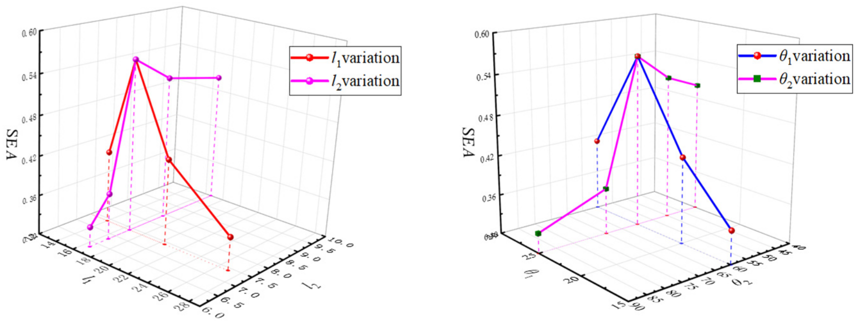

(**a**) (**b**)

Figure 19. Effect on SEA of DT-AHSs under comparison: (**a**) l_1 (l_2) value affects SEA, (**b**) θ_1 (θ_2) value affects SEA.

5. Conclusions

A series of comparative quasi-static compression tests on riveted and assembled DT-AHSs, 2D-DHSs, and CHHSs demonstrate the superior performance of the DT-AHSs. Additionally, a parametric analysis of the DT-AHSs reveals the following key findings:

1. When compressed, the θ_1 and θ_2 of the unit cells change first when l_1 and l_2 are rotated and bent; when there is no internal pores of the honeycomb structure, l_1 and l_2 begin to yield and deform.
2. In the initial small deformation stage, the bending moment drives cell wall deformation, with compressive displacement primarily resulting from rotational effects. When $\theta_2 > 90°$, the cell exhibits positive Poisson's ratio characteristics; when $\theta_2 < 90°$, auxetic behavior is observed.
3. The DT-AHSs demonstrates higher E^*, σ_{pl}, and SEA compared to the 2D-DHSs and CHHSs. A distinct plateau stress enhancement zone is observed, accompanied by typical auxetic effects. Although the ρ_{area} of the DT-AHSs is 3.9% greater than the average, its SEA is 107.4% higher.
4. An increase in cellular layers enhances load uniformity, extends the plateau segment, and amplifies the stress enhancement zone. While E^*, σ_{p}, and σ_{pl} decrease, SEA significantly improves.
5. The long inclined walls (l_1) of the DT-AHSs cells has a more pronounced effect on the energy dissipation properties than the short inclined walls (l_2). The plastic yield deformation of l_1 absorbs a substantial amount of impact energy. Meanwhile, the rotational deformation of l_2 contributes to both enhanced energy dissipation and the structure's auxetic behavior.

Author Contributions: Z.T.: data curation, writing—original draft, methodology. S.S.: conceptualization, funding acquisition, writing—review and editing. Y.L.: conceptualization, funding acquisition, writing—review and editing. W.W.: investigation, formal analysis, data curation. L.Z.: formal analysis, data curation, visualization. Y.X.: investigation, formal analysis, supervision. All authors have read and agreed to the published version of the manuscript.

Funding: This research was funded by the National Natural Science Foundation of China grant number 12302453, China Postdoctoral Science Foundation grant number 2022M723862, and the Chongqing Natural Science Foundation grant number CSTB2022NSCQ-MSX0188, Logistics key projects grant number. BLJ23J008.

Data Availability Statement: Data is unavailable due to privacy or ethical restrictions.

Acknowledgments: This work was financially supported by the National Natural Science Foundation of China (Grant No. 12302453), China Postdoctoral Science Foundation (Grant No. 2022M723862), and the Chongqing Natural Science Foundation (Grant No. CSTB2022NSCQ-MSX0188), Logistics key projects (Grant No. BLJ23J008). The authors would like to express their thanks.

Conflicts of Interest: The authors declare that they have no known competing financial interests or personal relationships that could have appeared to influence the work reported in this paper.

References

1. Nguyen, D.D.; Pham, C.H. Nonlinear dynamic response and vibration of sandwich composite plates with negative Poisson's ratio in auxetic honeycombs. *J. Sandw. Struct. Mater.* **2018**, *20*, 692–717. [CrossRef]
2. Chen, C.; He, Y.; Xu, R.; Gao, C.; Li, X.; Lu, M. Dynamic behaviors of sandwich panels with 3D-printed gradient auxetic cores subjected to blast load. *Int. J. Impact Eng.* **2024**, *188*, 104943. [CrossRef]
3. Guo, K.; Zhu, L.; Li, Y.; Yu, T.X. Numerical study on mechanical behavior of foam core sandwich plates under repeated impact loadings. *Compos. Struct.* **2019**, *224*, 111030. [CrossRef]
4. Zhang, W.; Yin, S.; Yu, T.X.; Xu, J. Crushing resistance and energy absorption of pomelo peel inspired hierarchical honeycomb. *Int. J. Impact Eng.* **2019**, *125*, 163–172. [CrossRef]
5. Fang, H.; Mao, Y.; Liu, W.; Zhu, L.; Zhang, B. Manufacturing and evaluation of Large-scale Composite Bumper System for bridge pier protection against ship collision. *Compos. Struct.* **2016**, *158*, 187–198. [CrossRef]
6. Baroutaji, A.; Sajjia, M.; Olabi, A.-G. On the crashworthiness performance of thin-walled energy absorbers: Recent advances and future developments. *Thin-Walled Struct.* **2017**, *118*, 137–163. [CrossRef]
7. Aghajani, S.; Wu, C.; Li, Q.; Fang, J. Additively manufactured composite lattices: A state-of-the-art review on fabrications, architectures, constituent materials, mechanical properties, and future directions. *Thin-Walled Struct.* **2024**, *197*, 111539. [CrossRef]
8. Ai, S.; Mao, Y.; Pei, Y.; Fang, D.; Tang, L. Study on aluminum honeycomb sandwich panels with random skin/core weld defects. *J. Sandw. Struct. Mater.* **2013**, *15*, 704–717. [CrossRef]
9. Lakes, R. Foam Structures with a Negative Poisson's Ratio. *Science* **1987**, *235*, 1038–1040. [CrossRef]
10. Lakes, R. Advances in negative Poisson's ratio materials. *Adv. Mater.* **1993**, *5*, 293–296. [CrossRef]
11. Evans, K.E.; Alderson, A. Auxetic Materials: Functional Materials and Structures from Lateral Thinking! *Adv. Mater.* **2000**, *12*, 617–628. [CrossRef]
12. Yang, Z.; Deng, Q. Mechanical property and application of materials and structures with negative poisson's ratio. *Adv. Mech.* **2011**, *41*, 3. (In Chinese)
13. Prawoto, Y. Seeing auxetic materials from the mechanics point of view: A structural review on the negative Poisson's ratio. *Comput. Mater. Sci.* **2012**, *58*, 140–153. [CrossRef]
14. Ma, Z.-D.; Bian, H.; Sun, C.; Hulbert, G.M.; Bishnoi, K.; Rostam-Abadi, F. Functionally-graded NPR (Negative Poisson's Ratio) material for a blast-protective deflector. In Proceedings of the 2010 Ndia Ground Vehicle Systems Engineering and Technology Symposium Modeling & Simulation, Testing and Validation (MSTV) Mini-Symposium, Dearborn, MI, USA, 17–19 August 2010.
15. Prall, D.; Lakes, R.S. Properties of a chiral honeycomb with a poisson's ratio of—1. *Int. J. Mech. Sci.* **1997**, *39*, 305–314. [CrossRef]
16. Jin, M.; Hou, X.; Zhao, W.; Deng, Z. Symplectic stiffness method for the buckling analysis of hierarchical and chiral cellular honeycomb structures. *Eur. J. Mech.—A/Solids* **2024**, *103*, 105164. [CrossRef]
17. Li, N.; Liu, S.; Zhang, X.; Zhang, Y.; Qi, W. Dynamic mechanical properties of novel star-rhombic negative Poisson's ratio honeycomb structure. *Acta Mater. Compos. Sin.* **2024**, *1000*, 3851. [CrossRef]
18. Xiao, D.; Kang, X.; Li, Y.; Wu, W.; Lu, J.; Zhao, G.; Fang, D. Insight into the negative Poisson's ratio effect of metallic auxetic reentrant honeycomb under dynamic compression. *Mater. Sci. Eng. A* **2019**, *763*, 138151. [CrossRef]
19. Larsen, U.D.; Signund, O.; Bouwsta, S. Design and fabrication of compliant micromechanisms and structures with negative Poisson's ratio. *J. Microelectromech. Syst.* **1997**, *6*, 99–106. [CrossRef]
20. Chen, G.; Cheng, Y.; Zhang, P.; Liu, J.; Chen, C.; Cai, S. Design and modelling of auxetic double arrowhead honeycomb core sandwich panels for performance improvement under air blast loading. *J. Sandw. Struct. Mater.* **2021**, *23*, 3574–3605. [CrossRef]
21. Qiu, X.M.; Zhang, J.; Yu, T.X. Collapse of periodic planar lattices under uniaxial compression, part I: Quasi-static strength predicted by limit analysis. *Int. J. Impact Eng.* **2009**, *36*, 1223–1230. [CrossRef]
22. Qi, C.; Jiang, F.; Yu, C.; Yang, S. In-plane crushing response of tetra-chiral honeycombs. *Int. J. Impact Eng.* **2019**, *130*, 247–265. [CrossRef]
23. Wei, L.; Zhao, X.; Yu, Q.; Zhang, W.; Zhu, G. In-plane compression behaviors of the auxetic star honeycomb: Experimental and numerical simulation. *Aerosp. Sci. Technol.* **2021**, *115*, 106797. [CrossRef]
24. Álvarez Elipe, J.C.; Díaz Lantada, A. Comparative study of auxetic geometries by means of computer-aided design and engineering. *Smart Mater. Struct.* **2012**, *21*, 105004. [CrossRef]
25. Hou, X.; Deng, Z.; Zhang, K. Dynamic Crushing Strength Analysis of Auxetic Honeycombs. *Acta Mech. Solida Sin.* **2016**, *29*, 490–501. [CrossRef]

26. Gao, Q.; Wang, L.; Zhou, Z.; Ma, Z.D.; Wang, C.; Wang, Y. Theoretical, numerical and experimental analysis of three-dimensional double-V honeycomb. *Mater. Des.* **2018**, *139*, 380–391. [CrossRef]
27. Liao, Y.; Shi, S.Q.; Xia, F.; Yang, W. Study on anti-explosion mechanical properties of double trapezoidal negative poisson's ratio auxetic sandwich honeycomb structure. *Eng. Mech.* **2023**, *41*, 1–18. (In Chinese)
28. Kaushik, R.K. *Strength of Materials*; I.K. International Publishing: Delhi, India, 2019; Chapter 21; pp. 425–433.
29. Zhou, H.; Zhang, X.; Wang, X.; Wang, Y.; Zhao, T. Response of foam concrete-filled aluminum honeycombs subject to quasi-static and dynamic compression. *Compos. Struct.* **2020**, *239*, 112025. [CrossRef]
30. Li, Z.; Yu, T.X.; Wan, L.; Zeng, Q.; Ruan, D. Non-dimensional parameters governing the crashworthy performance of tubes with complex cross-sections. *Int. J. Mech. Sci.* **2024**, *278*, 109476. [CrossRef]
31. Habib, F.N.; Iovenitti, P.; Masood, S.H.; Nikzad, M. Fabrication of polymeric lattice structures for optimum energy absorption using Multi Jet Fusion technology. *Mater. Des.* **2018**, *155*, 86–98. [CrossRef]
32. Nickabadi, S.; Sayar, M.A.; Alirezaeipour, S.; Ansari, R. Optimizing an auxetic metamaterial structure for enhanced mechanical energy absorption: Design and performance evaluation under compressive and impact loading. *J. Sandw. Struct. Mater.* **2024**, *26*, 1129–1164. [CrossRef]
33. Galehdari, S.A.; Kadkhodayan, M.; Hadidi-Moud, S. Low velocity impact and quasi-static in-plane loading on a graded honeycomb structure; experimental, analytical and numerical study. *Aerosp. Sci. Technol.* **2015**, *47*, 425–433. [CrossRef]
34. Hou, B.; Wang, Y.; Sun, T.F.; Liu, J.G.; Zhao, H. On the quasi-static and impact responses of aluminum honeycomb under combined shear-compression. *Int. J. Impact Eng.* **2019**, *131*, 190–199. [CrossRef]